

PAPER • OPEN ACCESS

# Measurement of laser powder bed fusion surfaces with light scattering and unsupervised machine learning



To cite this article: Mingyu Liu *et al* 2022 *Meas. Sci. Technol.* **33** 074006

View the [article online](#) for updates and enhancements.

You may also like

- [Powder thermal conductivity measurements in laser powder-bed fusion: an uncertainty study with sensitivity analysis](#)  
Shanshan Zhang, Brandon Lane and Kevin Chou
- [A mesoscopic digital twin that bridges length and time scales for control of additively manufactured metal microstructures](#)  
Tae Wook Heo, Saad A Khairallah, Rongpei Shi et al.
- [Molten pool structure and temperature flow behavior of green-laser powder bed fusion pure copper](#)  
Pan Lu, Zhang Cheng-Lin, Liu Tong et al.

# Measurement of laser powder bed fusion surfaces with light scattering and unsupervised machine learning

Mingyu Liu<sup>1,\*</sup> , Nicola Senin<sup>1,2</sup> , Rong Su<sup>3</sup> and Richard Leach<sup>1</sup>

<sup>1</sup> Manufacturing Metrology Team, Faculty of Engineering, University of Nottingham, Nottingham, United Kingdom

<sup>2</sup> Department of Engineering, University of Perugia, Perugia, Italy

<sup>3</sup> Shanghai Institute of Optics and Fine Mechanics, Chinese Academy of Sciences, Shanghai 201800, People's Republic of China

E-mail: [mingyu.liu1@nottingham.ac.uk](mailto:mingyu.liu1@nottingham.ac.uk)

Received 25 November 2021, revised 22 March 2022

Accepted for publication 7 April 2022

Published 21 April 2022



CrossMark

## Abstract

Quality monitoring for laser powder bed fusion (L-PBF), particularly in-process and real-time monitoring, is of importance for part quality assurance and manufacturing cost reduction. Measurement of layer surface topography is critical for quality monitoring, as any anomaly on layer surfaces can result in defects in the final part. In this paper, we propose a surface measurement method, based on the use of scattered light patterns and a convolutional autoencoder-based unsupervised machine learning method, designed and trained using a large set of scattering patterns simulated from reference surfaces using a scattering model. The advantage of using an autoencoder is that the monitoring model can be trained using solely data from acceptable surfaces, without the need to ensure the presence of representative observations for all the types of possible surface defects. The advantage of using simulated data for training is that we can obtain an effective monitoring solution without the need for a large collection of experimental observations. Here we report the results of a preliminary investigation on the performance of the proposed solution, where the trained autoencoder is tested on experimental data obtained off-process, using a dedicated experimental apparatus for generating and collecting light scattering patterns from manufactured L-PBF surfaces. Our results indicate that the proposed monitoring solution is capable of detecting both acceptable and anomalous surfaces. Although further validation is required to fully assess performance within an on-machine and in-process setup, our preliminary results are encouraging and provide a glimpse of the potential benefits of using our surface measurement solution for L-PBF in-process monitoring.

Keywords: laser powder bed fusion, surface measurement, light scattering, unsupervised machine learning

(Some figures may appear in colour only in the online journal)

\* Author to whom any correspondence should be addressed.



Original content from this work may be used under the terms of the [Creative Commons Attribution 4.0 licence](https://creativecommons.org/licenses/by/4.0/). Any further distribution of this work must maintain attribution to the author(s) and the title of the work, journal citation and DOI.

## 1. Introduction

Laser powder bed fusion (L-PBF) with metal materials is playing an important role within modern additive manufacturing (AM) in numerous applications spanning various fields, such as aerospace, automotive and biomedical [1]. L-PBF has been showing excellent performance and capability for producing highly complex geometries [1, 2]. To ensure the quality of L-PBF built parts, as well as to reduce cost, defects and other deviations of L-PBF layer surfaces, there is increased interest in monitoring during the process, particularly for parts with stringent quality requirements [3, 4]. Any anomaly generated on a layer surface during the process may eventually lead to quality issues or even functional/structural failure in the final parts [5].

In-process measurement of L-PBF surfaces introduces challenging requirements such as the need for high measurement speed (to avoid slowing down the process, thus altering temperatures and other process conditions), long working distances (to avoid physical interference with the laser and other components within the build chamber) and robustness to harsh environments (due to the laser, presence of gases, plasma and particles). Two-dimensional (2D) optical imaging of the layer has been applied [6–10]; the primary advantage being high measurement speed. The main issue with imaging is the interpretational challenge, as the discernible image features are influenced by illumination, shadows, varying contrast and other sources of noise. Infrared imaging has also been used to detect anomalies in layer surfaces [11, 12]. Optical, three-dimensional (3D) areal topography measurement technologies capable of reaching high spatial sampling resolutions (such as coherence scanning interferometry, focus variation microscopy and confocal imaging microscopy) have the advantage of providing a 3D reconstruction of layer topography, thus removing most of the disadvantages associated with 2D image interpretation. However, such technologies are difficult to apply on-machine or in-process, due to the harsh operating environments, scarce robustness to noise and the requirement for fast sampling rates [13, 14]. At larger spatial scales, other optical technologies, such as fringe projection and photogrammetry are being investigated [15–17], but have similar challenges and limitations to those for higher-resolution technologies, and have the additional downside of not being able to capture information related to the smaller topographic features, for example the ripples present on the weld tracks of L-PBF layers [18]. Methods based on combining different sensors have also been developed to measure layer surfaces. For example by combining a high-speed camera and a two-colour pyrometer to investigate the laser consolidation process [10]; combining a high-speed camera and a photodiode for quality control of the selective laser melting process [9]; using a visible light photodiode and infrared light photodiode integrated into the laser module of the L-PBF machine for fault detection [19, 20]; or using multiple sensors of the same kind, such as the combination of two photodiodes to capture scattered light from different locations in the build chamber, together with the location of the laser spot position to detect lack of fusion porosity in an L-PBF process [21, 22].

Currently, research on in-process monitoring for L-PBF layer surfaces is still active and new techniques are being developed to meet the stringent requirements, improve performance and reduce costs [2].

We have previously developed a method to detect defects on surfaces featuring regular topographic patterns (e.g. gratings), based on using a light source to illuminate the surface, collect the scattered reflection pattern by using a sensor array, and finally analyse the pattern using machine learning to perform pattern classification and thus detect anomalies [23–25]. We have shown that using machine learning can solve the complex inverse scattering problem efficiently (compared to the traditional library search method [26]) and our solution based on combining light scattering and machine learning is relatively fast (compared to fringe projection methods [15, 16]), thus suitable for application to in-process monitoring, and introduces minimal concerns in terms of process disturbance or accessibility issues. In addition, we have shown that the training for machine learning can be accomplished using numerical simulation to generate artificial scattering patterns, which is more efficient than collecting a large number of real ones [27, 28]. However, the previously proposed solution could only rely on 2D scattering simulation for training (i.e. training datasets would consist of light intensities scattered on a 2D cross-sectional plane, and collected onto an arc-shaped trajectory) and, therefore, could only process topographies whose scattered reflection could be suitably represented by 2D patterns, e.g. one-directional topographies such as gratings. In this work, as complex and intrinsically 3D L-PBF surfaces are addressed, the introduction of a 3D scattering model is required, which is far more computationally intensive. Equivalently, the need to address a multitude of diverse anomalies which could be featured by a fully 3D topography, such as that typical of L-PBF, makes it inconvenient to adopt machine learning strategies that require training examples for all the possible classes of anomalies. Therefore, an unsupervised machine learning model based on an autoencoder is selected, only requiring observations from acceptable surface states for training, and designed to detect anomalous states as departures from acceptable ones.

In summary, this paper proposes a measurement method for L-PBF surfaces using light scattering and unsupervised learning. The light scattering data for training of the machine learning model is generated by 3D scattering simulations, using reference geometric models of L-PBF surfaces which are considered to have acceptable surface topography. The simulation is based on the Kirchhoff approximation (see section 2.2) which makes the 3D computations feasible as opposed to running a more rigorous (and more computationally intensive) model based on the boundary element method (BEM) [29]. The machine learning model is based on a convolutional autoencoder. The autoencoder learns to efficiently encode and decode the scattering patterns belonging to the reference surfaces. Using the trained autoencoder, an automated detector of anomalies can be built by monitoring the reconstruction error generated by the autoencoder, which is higher when a non-reference pattern is processed instead. To assess the performance of the proposed solution, the convolutional

autoencoder, trained over simulated scattering patterns representative of acceptable L-PBF surfaces, is tested using new sets of simulated patterns belonging to acceptable and anomalous topographies, but also through an experimental campaign where the trained autoencoder is fed with real scattering patterns obtained by a special-purpose experimental apparatus, and generated from both acceptable and anomalous physical surface samples. The validation confirms the effectiveness of the solution based on combining light scattering and the convolutional autoencoder for detecting anomalous L-PBF surfaces, and paves the way for future developments where the solution will be tested in-process, using scattering patterns generated and collected during operation within the build chamber of a real L-PBF machine. To the best of our knowledge, this work is the first attempt to use light scattering combined with machine learning to measure L-PBF surfaces.

## 2. Methods and materials

A schematic diagram of the proposed method is shown in figure 1. Laser light (LS) is projected to the targeted L-PBF surface, reflected by the surface, captured by a sensor and recorded in the form of a light scattering pattern (an intensity image), and finally fed into a pattern classifier powered by machine learning (a convolutional autoencoder). As also shown in figure 1, scattering patterns to be fed into the classifier can be input from numerical simulation.

### 2.1. Design of the unsupervised machine learning model (autoencoder)

The machine learning model is designed as a convolutional autoencoder, which is an unsupervised machine learning model. The structure of the autoencoder is shown in figure 2. The input of the autoencoder is a large set of scattering patterns simulated using geometric models of reference L-PBF surfaces. These geometric models have been obtained by firstly generating physical surface specimens using L-PBF with optimal process parameters and in control conditions, and secondly by acquiring the topography of such specimens by using a coherence scanning interferometer (CSI) areal topography measuring instrument [30]. Once the geometric models of topography are available, a 3D simulation can be used to project a virtual laser beam onto the surface and reconstruct its scattered reflection. Details of the simulation are provided in section 2.2.

Each simulated scattering pattern is collected within an image of  $200 \times 200$  pixels, and becomes an observation within the set used to train the autoencoder. In the encoding part of the convolutional autoencoder, the patterns are processed by three convolutional layers, each followed by a downsampling step. The first, second and third convolutional layers are designed as 16, 12 and 8 filters, each with a kernel size of  $3 \times 3$ . As a result, the shape of the data is changed from  $200 \times 200$  to  $100 \times 100 \times 16$ ,  $50 \times 50 \times 12$  and  $25 \times 25 \times 8$ , respectively. A flatten layer is then used to reshape the data from  $25 \times 25 \times 8$  to  $5000 \times 1$ , which is essentially a 1D array, densely connected with a layer of 1024 nodes, representing the

final result of the encoding process. In the decoding part of the autoencoder, the 1024 node data is first connected to another densely connected layer with 5000 nodes and then reshaped to a grid of  $25 \times 25 \times 8$  pixels. The data is then further processed by three transposed convolutional layers, each followed by an upsampling process. The first, second and third convolutional layers in the decoding process are designed as 8, 12 and 16 filters, each with a kernel size  $3 \times 3$ . The decoding process is essentially the inverse of the encoding process and the size of the data is changed from  $25 \times 25 \times 8$  to  $50 \times 50 \times 12$ ,  $100 \times 100 \times 16$  and eventually  $200 \times 200$ , which corresponds to the size of the original input data and represents the final result of the decoding process.

The performance of an autoencoder is quantified by the quality of reconstruction, i.e. how small the error (difference) is between the original and the reconstructed datasets. The same error is used as the minimisation target for the training function; more specifically through the loss function, defined as the mean squared error of the differences between the original and reconstructed datasets. A trained autoencoder is, therefore, capable of encoding the input dataset into an optimal set of features (learned by training), and decoding such features back into an output (the reconstructed dataset) that is as close as possible to the original dataset. To train the model, we only use the data from reference surfaces representative of acceptable surface states; the autoencoder is fitted to a condition of optimal performance that applies only to surfaces similar to the reference. Anomalous surfaces generating input data with large deviations with respect to the reference are encoded and decoded poorly, resulting in larger reconstruction errors. The observation of an unexpected reconstruction error in the operation of the autoencoder can, therefore, be used as an indication that an anomalous surface has been encountered (or at least, a surface with significant differences from the references). In this work, the convolutional autoencoder was implemented in TensorFlow/Keras and the training was performed on a supercomputer (Augusta) with 2 Nvidia V100 GPUs, under the high performance computing (HPC) service provided by the University of Nottingham.

### 2.2. Generation of training datasets

The datasets (light scattering patterns) used for training the convolutional autoencoder were artificially generated by using a 3D scattering simulation [31]. The simulation was based on using digital, geometric models of surface topography, obtained from areal topography data acquired by measuring three real L-PBF surfaces, one of which was visually assessed as acceptable and used as a reference, the other two being representative of anomalous states. Areal topography measurement was performed by CSI (Zygo Nexview NX2). The method of generation of the training datasets is illustrated in figure 3. A relatively large area ( $1400 \times 1400$ )  $\mu\text{m}$  for the originally selected reference L-PBF surfaces (representing acceptable surface topography) was initially acquired. Then smaller surface regions were extracted at different locations of

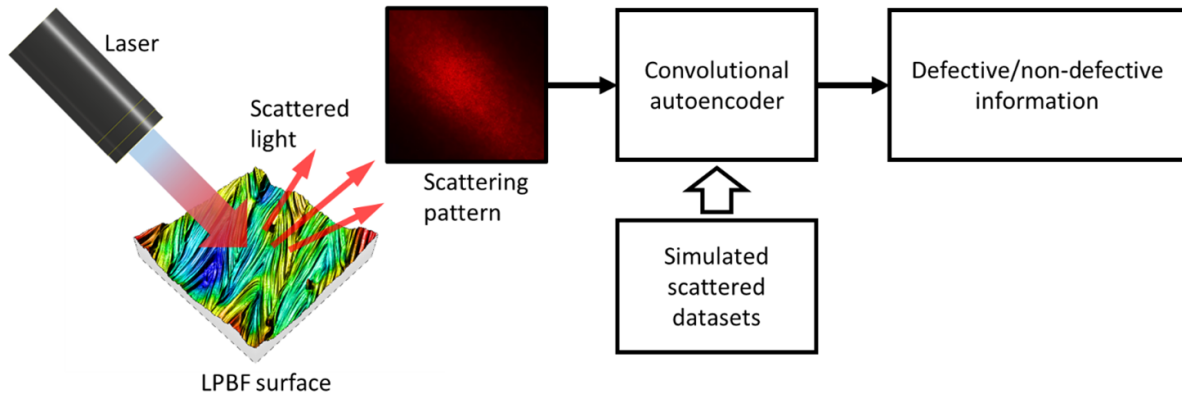


Figure 1. Diagram of the proposed method.

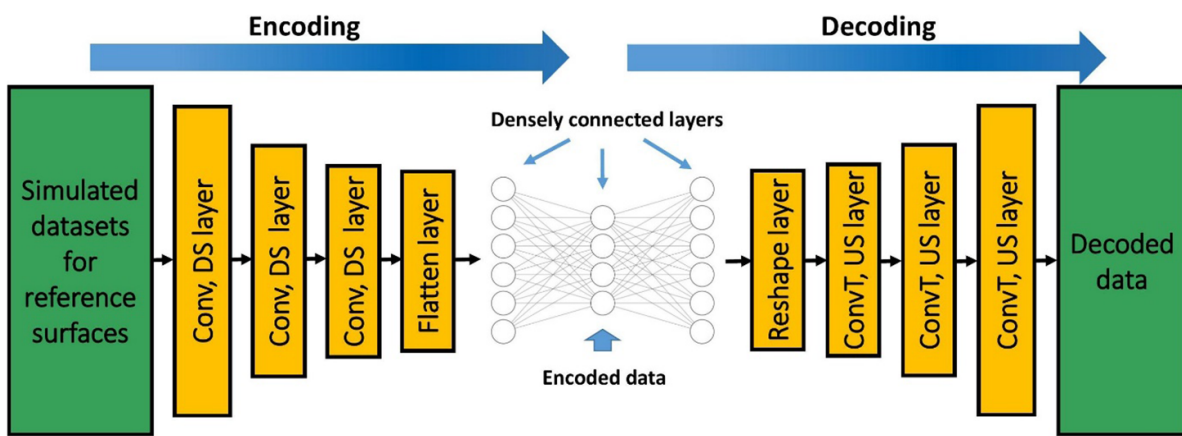


Figure 2. Convolutional autoencoder, Conv: convolutional, ConvT: transpose convolutional, DS: downsampling, US: upsampling.

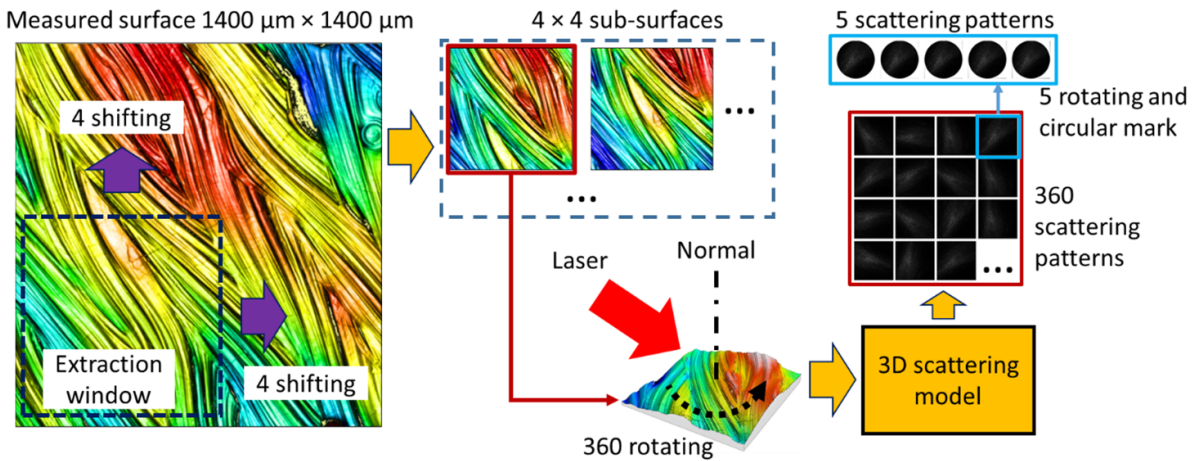
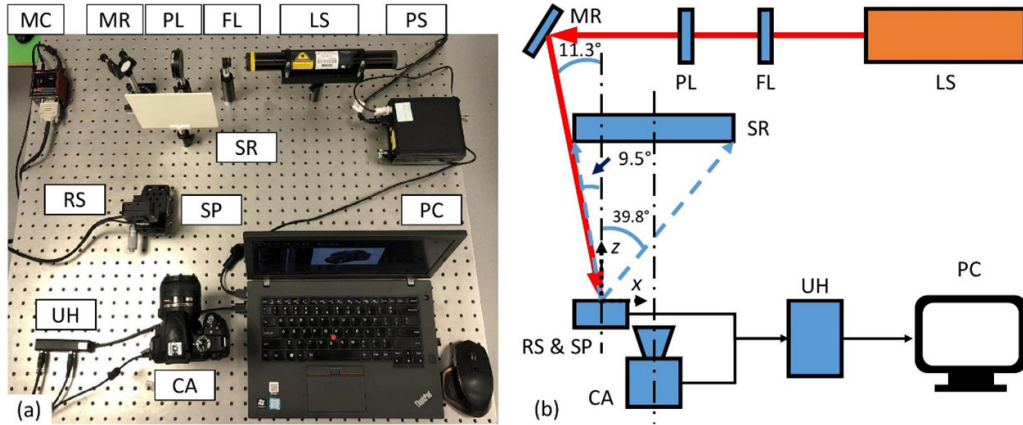


Figure 3. Generation of the training datasets.

each area, by shifting the extraction window in both  $x$  and  $y$  directions four times, leading to 16 extracted regions in total. All the topography datasets were fed into a 3D scattering model based on the Kirchhoff approximation [31], to generate the scattering patterns. The resolution of the generated patterns was  $200 \times 200$  pixels. The simulations were repeated multiple times, by rotating each surface about its normal,  $1^\circ$  at a time, so that the incidence direction of the projected LS

(virtual) would change, leading to 360 simulated scattering patterns per surface. The resulting scattering patterns were further multiplied by rotating five steps at  $0.2^\circ$  intervals on the pattern plane. A circular mask was applied to make the effective area rotationally symmetric (as the original scattering pattern was collected into a square detector). As a result, we obtained  $16 \times 360 \times 5 = 28\,800$  training datasets. The simulated scattering patterns were then intensity-normalised to a



**Figure 4.** Experiment setup, (a) actual setup, and (b) schema.

0 to 1 interval. The numerical simulation was implemented in Matlab and executed using the parallel processing capabilities provided by the HPC service, as detailed in section 2.1.

### 2.3. Verification of scattering simulation

The major limitation of the scattering model used in this study is the validity regime of the Kirchhoff approximation. To verify the accuracy of the scattering simulation model for the target surface (L-PBF surfaces used in this work), we adopt the method used in our previous work [32]—the criterion proposed by Brekhovskikh (section 3.3 in [33]):

$$C_R = \frac{4\pi r_C \cos \theta}{\lambda} \gg 1 \quad (1)$$

where  $r_C$  is the radius of curvature at a surface point and  $\theta$  is the local angle of incidence. Furthermore, we compare the result from the Kirchhoff approximation-based scattering model to the BEM [34], which is a rigorous model that can accurately simulate rough surface scattering and has been verified in our previous work [23] (the BEM, however, is more computationally intensive, particularly the 3D version [29]).

### 2.4. Experimental setup

After having trained the autoencoder with simulated data, we devised an experimental setup to collect real scattering patterns from real L-PBF surfaces for the purpose of testing the autoencoder. The experimental setup is shown in figure 4. It should be noted that the setup does not allow us to obtain a perfect replica of the scattering patterns that would be obtained when operating in-process within the build chamber of a L-PBF machine for the following reasons:

- the surrounding atmosphere for the experimental setup is a laboratory atmosphere, not the typical atmosphere of gases and flying particles/spatter commonly found in L-PBF;
- the surfaces measured in the experimental setup belong to physical L-PBF specimens and represent completed surfaces; on the contrary, in-process, a surface featuring a

- mixture of laser-processed regions and surrounding unprocessed powders would be targeted; and
- different to a laboratory environment, operating in the build chamber would imply the presence of additional sources of disturbance, e.g. vibration of the machine and processing laser.

In figure 4(a) the experimental setup is shown and a schema is shown in figure 4(b). The laser light (LS), with a wavelength of approximately 633 nm and a diameter of approximately 0.8 mm, is projected to a mirror (MR) through a neutral density filter (FL) and a polariser (PL) before reflecting onto the measured L-PBF sample (SP). The sample is mounted on a rotational stage (RS), to investigate the effects of different surface orientations on the reflection. The scattered light is collected by a screen (SR, 150 mm × 150 mm) and captured by a camera (CA). The RS is driven by a motion controller (MC). MC and CA are controlled through a USB hub (UH) connected to a PC. The angle of the incident light to the normal of the L-PBF surface is 11.3°. The range of angles of the scattered light captured by the screen varies from  $-9.5^\circ$  to  $39.8^\circ$ , with respect to the  $x$  direction. In the  $y$  direction (normal to the figure plane), the centre of the screen is aligned to the centre of the L-PBF sample surface, so that scattered reflections can be captured within the range  $-26.5^\circ$  to  $+26.5^\circ$  (not shown in the figure) with respect to the  $y$  direction. The geometric arrangement of the experimental setup corresponds to what was adopted in the 3D scattering simulation to generate datasets to train the convolutional autoencoder.

## 3. Results and discussion

Figure 5 shows the topographies of the three L-PBF surfaces measured separately using CSI. Each measurement was performed with a  $50\times$  objective resulted in  $(1 \times 1)$  mm areal topography data, cropped to  $(400 \times 400)$   $\mu\text{m}$  for better visualisation. The manufacturing process parameters for the L-PBF surfaces are shown in table 1. The AM1 surface was manufactured using optimal manufacturing process parameters while AM2 and AM3 were manufactured using different

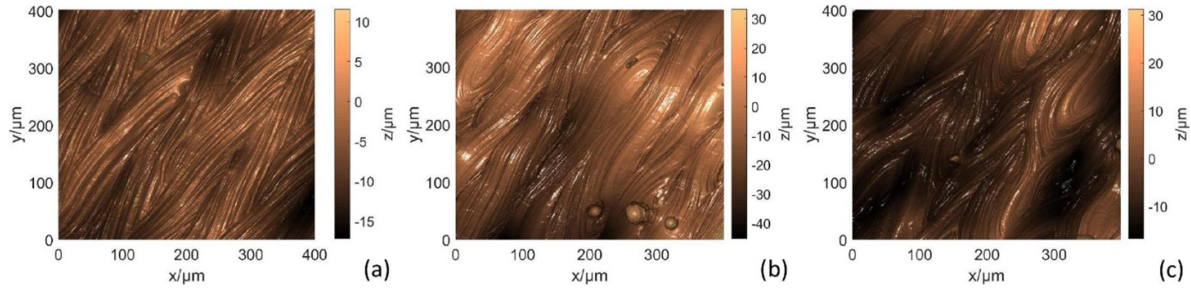


**Figure 5.** L-PBF AM surfaces for experiment, (a) AM1, (b) AM2, and (c) AM3.

**Table 1.** Manufacturing process parameters for the L-PBF surfaces.

	Laser power (W)	Scan speed ( $\text{m s}^{-1}$ )	Energy density ( $\text{J mm}^{-2}$ )
AM1	170	1.1	2.1
AM2	170	1.7	1.3
AM3	120	1.1	1.5

scan speeds and laser powers. The topographies reported in figure 4 clearly show that the AM1 surface, manufactured with optimal parameters, has finer texture distributed all over the surface, while AM2 and AM3 have unevenly distributed textures and larger hump-like features, which may be caused by insufficient energy density applied on the powder bed (with faster scan speed and/or lower laser power). As a result, the AM1 surface was used as the reference surface, whilst AM2 and AM3 were used as representative of out-of-control states.

### 3.1. Verification results of the scattering simulation

The verification results for the scattering simulations are presented in this section. Parameters for the scattering simulations, such as the wavelength of LS and incident angle, are summarised in table 2 and the results are shown in figure 6. Figure 6(a) is an extracted profile from the L-PBF surface (AM1). Figure 6(b) is the power density distribution of the local angle of incidence of the profile, which shows the majority of the local angles of incidence are less than  $40^\circ$ . Figure 6(c) is the power density distribution of the coefficient  $C_R$ , which shows that only a small number (less than 1%) of locations in the profile have  $C_R$  values smaller than 10, indicating that the scattering model (Kirchhoff approximation) should be accurate for the L-PBF surfaces used in this work. Figures 6(d) and (e) show the scattering patterns simulated from the Kirchhoff approximation-based scattering and BEM models, where the results are in good agreement, showing the Kirchhoff approximation-based scattering model used in this work can effectively simulate the scattering patterns for these L-PBF surfaces. Due to the complexity of the L-PBF surfaces and the scattering patterns, the scattering patterns were compared qualitatively as it was difficult to do a quantitative comparison. A comparison has been done for the Kirchhoff approximation and the BEM for relatively simple 2D profiles

**Table 2.** Simulation parameters.

Wavelength of incident light	633 nm
Incidence angle	Normal
Length of profile	400 $\mu\text{m}$
Far field distance	100 mm

[35] and a comprehensive comparison study for the Kirchhoff approximation and the BEM using simpler 3D surfaces will be conducted in future work.

### 3.2. Simulation results

In figure 7, the simulated scattering patterns for surfaces AM1, AM2, and AM3 are shown. The simulation was carried out with an incidence angle of  $11.3^\circ$ , the wavelength of incident light was 633 nm, as consistent with the actual experimental setup. The result for the AM1 surface shows a narrow, long stride pattern while those for AM2 and AM3 show wider stride patterns, which are consistent with the experimental results presented in the following section.

After the machine learning model was trained, simulated scattering patterns from surfaces AM1 and AM2 were used to test the model (autoencoder). Figure 8 shows one set of results of a scattering pattern simulated for surface AM1. In figure 8(a) the original scattering pattern is shown. Figure 8(b) shows the decoded scattering pattern, and figure 8(c) shows the deviation from the decoded and original scattering patterns. The decoded scattering pattern is a blurred version of the original scattering pattern. The results show that the deviations are relatively small and evenly distributed in the image, particularly where the scattering signal is visible, indicating that the machine learning model has learned the scattering patterns and effectively encodes/decodes the pattern.

Figures 9 and 10 show the results for surface AM2 and surface AM3. Figures 9(a) and 10(a), figures 9(b) and 10(b), figures 9(c) and 10(c) are the original scattering patterns, the decoded scattering patterns, and the deviations from the decoded scattering patterns to the original scattering patterns (i.e. reconstruction error), respectively. Compared to the results for surface AM1, the decoded scattering images are not only blurred but also features a different pattern. As a result, relatively large reconstruction errors can be observed, which are due to the fact that these datasets were not used in the

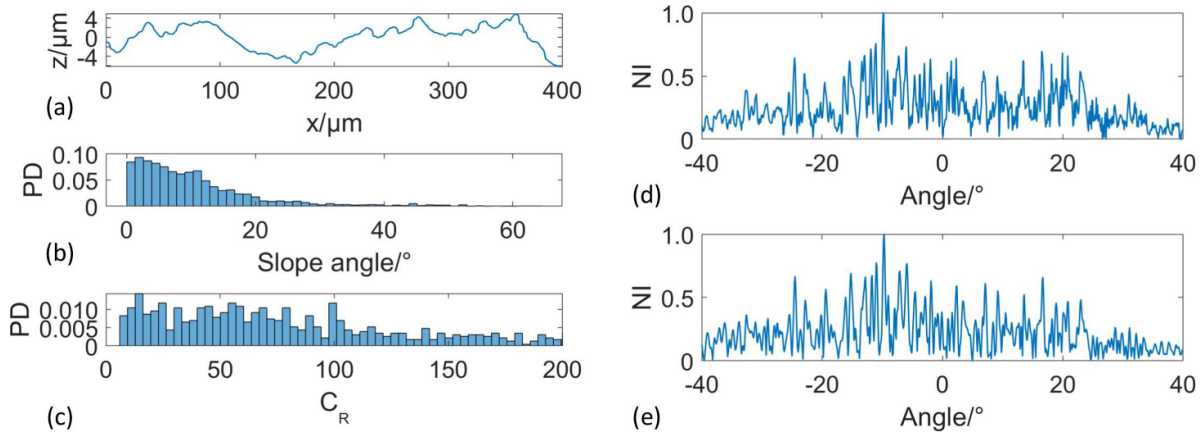


**Figure 6.** Validation result of the scattering model, (a) profile extracted from AM1 surface, (b) power density distribution of the slope angle of the profile, (c) power density distribution of the coefficient  $C_R$ , (d) scattering pattern simulated from the scattering model (Kirchhoff approximation), and (e) scattering pattern simulated from a rigorous model (BEM). PD: power density distribution, NI: normalised intensity.

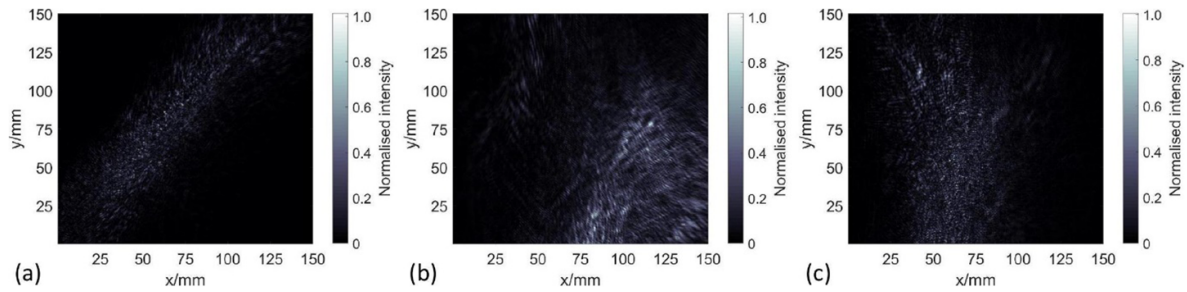


**Figure 7.** Simulated scattering patterns for (a) AM1, (b) AM2, and (c) AM3.

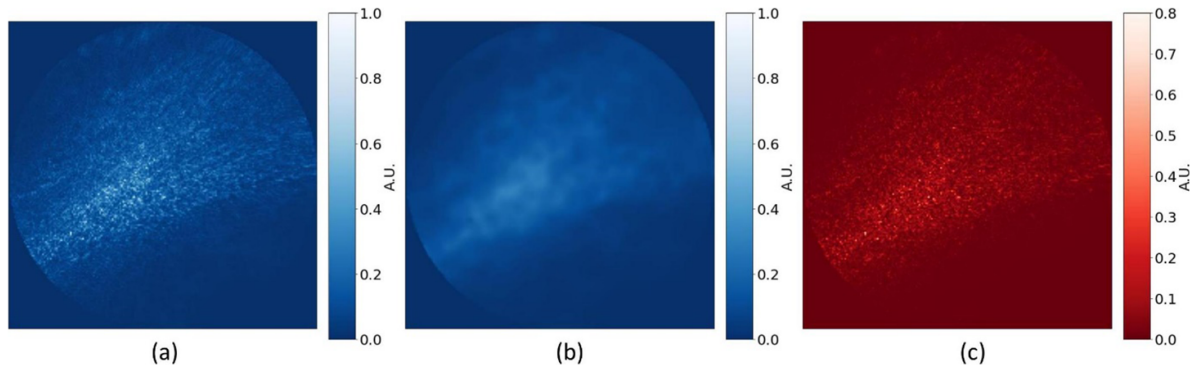


**Figure 8.** Testing result of a simulated scattering pattern for AM1 surface, (a) original scattering image, (b) decoded scattering image, and (c) deviation map. All subfigures are  $(150 \times 150)$  mm.

training process and hence the autoencoder could not effectively encode/decode them.

All the reconstruction errors from the numerical simulations (5760 sets) are summarised in a histogram of RMS values as well as their kernel density estimation (KDE, shown in solid lines as fitting of the histogram data) [36], as shown in figure 11. The results for surface AM1 have a smaller mean RMS error distribution, while those of AM2 and AM3 are distributed with a larger mean value. Thresholding with the value of the RMS errors for the data from surface AM1 provides a likelihood to identify to which surface the scattering patterns belong (except for the overlapping regions). For instance, by

setting a threshold as 0.053, i.e. if the RMS error is less than 0.053, the measured surface is classified as a non-defective surface, otherwise, it is classified as a defective surface. As a result, 5083 and 677 datasets from the reference surface were classified as non-defective and defective, respectively. On the other hand, 5655 and 105 datasets from the Defective1 surfaces were classified as defective and non-defective surfaces; 4690 and 1070 datasets from the Defective2 surfaces were classified as defective and non-defective surfaces. A confusion matrix can then be summarised as shown in table 3. The overall accuracy of the classifier is 89.3%, indicating that the proposed method has good performance for these simulation datasets.



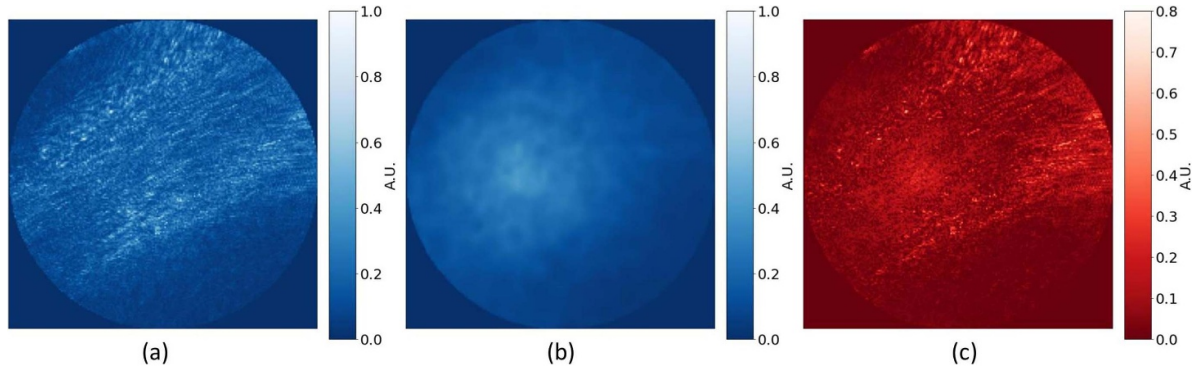


**Figure 9.** Testing results of simulated scattering patterns for AM2 surface, (a) original scattering image, (b) decoded scattering image, and (c) deviation map. All subfigures are  $150 \times 150$  mm.

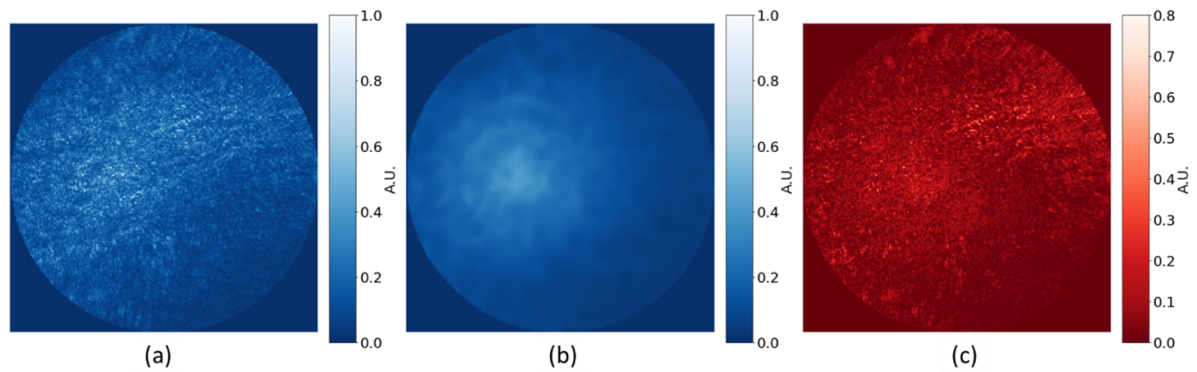


**Figure 10.** Testing results of simulated scattering patterns for AM3 surface, (a) original scattering image, (b) decoded scattering image, and (c) deviation map. All subfigures are  $150 \times 150$  mm.

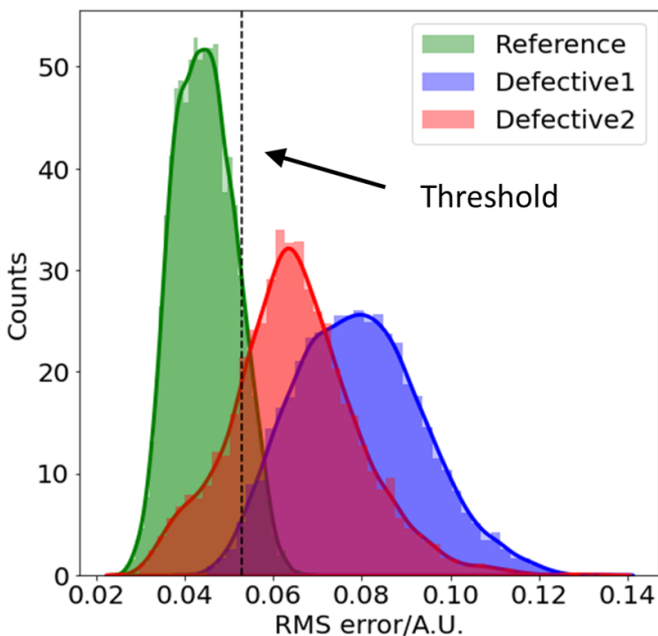


**Figure 11.** Testing results for the reference and target surfaces using simulated datasets.

Note that the determination of the threshold was based on the principle of maximisation of the accuracy using the simulation data. In practice, the selection of the threshold should be

**Table 3.** Confusion matrix for the simulation data.

	Predicted:	
	Non-defective	Defective
Actual: Non-defective	5083	677
Actual: Defective	105 + 1070 = 1175	5655 + 4690 = 10345

determined using the testing data from the experiment, which can be different from the simulation data due to the limited accuracy of the simulation model (this will be discussed in section 3.3).

### 3.3. Experimental results

Figures 12–14 show one set of testing results for surfaces AM1, AM2 and AM3, respectively, using the scattering patterns measured by the designed experimental apparatus. For each figure, subfigures (a)–(c) are the images for the original scattering pattern, decoded scattering pattern and reconstruction error, respectively. The results show that the reconstruction error for the reference surface—AM1 is smaller than those for the surfaces AM2 and AM3. While the scattering patterns for surface AM1 show long and narrow strides, those for AM2 and AM3 have wider patterns almost filling the whole image, consistent with the simulation results.

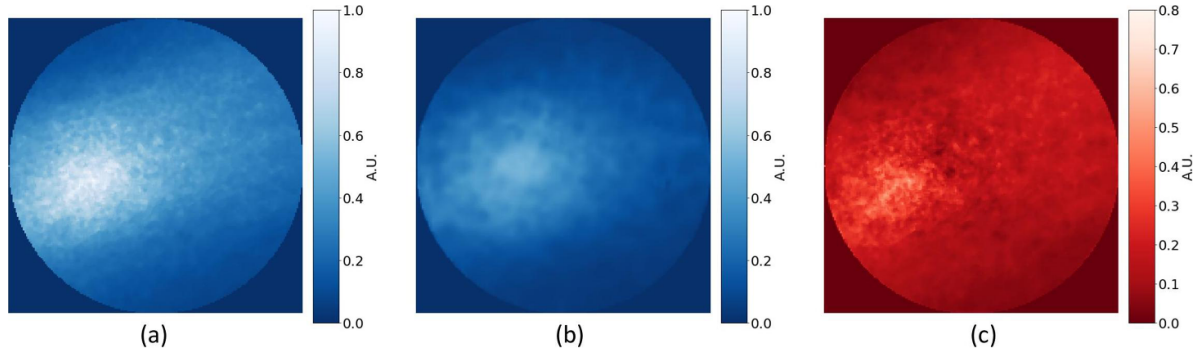


**Figure 12.** Testing surfaces AM1, (a) original scattering images, (b) decoded scattering images, and (c) deviation maps. All subfigures are (150 × 150) mm.

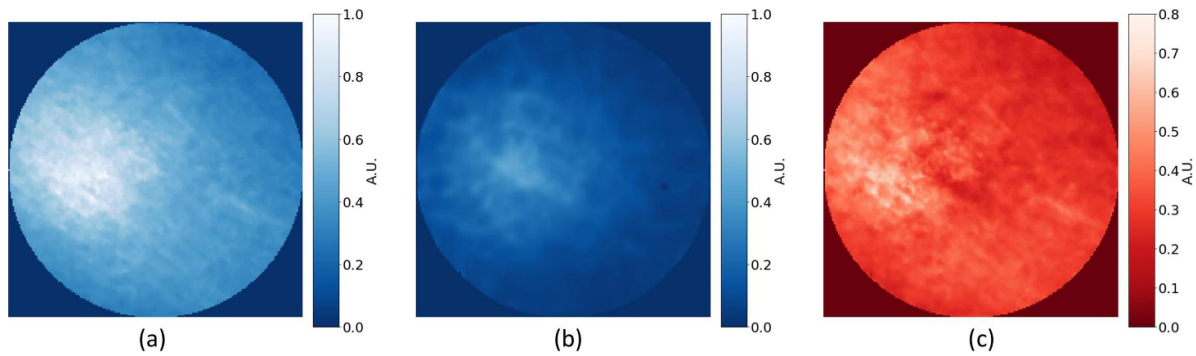


**Figure 13.** Testing surfaces AM2, (a) original scattering images, (b) decoded scattering images, and (c) deviation maps. All subfigures are (150 × 150) mm.

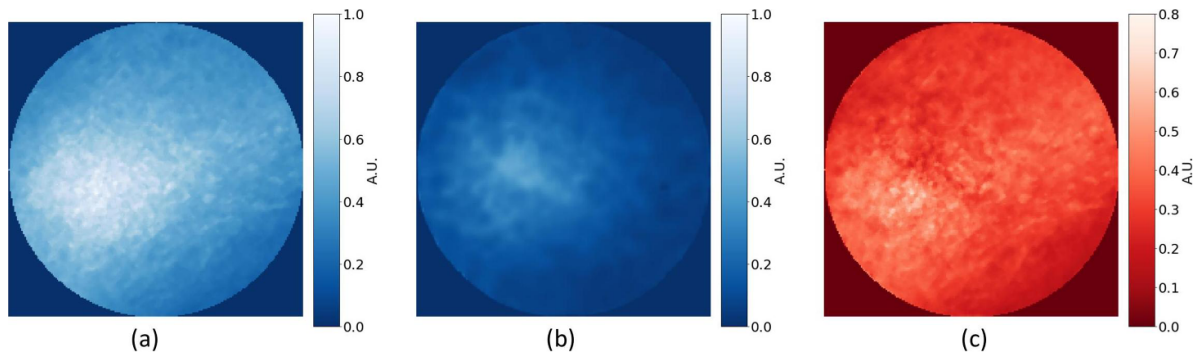


**Figure 14.** Testing surfaces AM3, (a) original scattering images, (b) decoded scattering images, and (c) deviation maps. All subfigures are (150 × 150) mm.

The results for the experiments are also summarised in the histogram shown in figure 15, as histograms and fitted KDE. Those for the reference surface AM1 have the smallest RMS error compared to those for AM2 and AM3. Thresholding on the RMS error can be used to determine whether the AM layer surfaces are being manufactured within the acceptable range, and thus to monitor the quality of the AM process. For example, by setting the threshold to 0.210, i.e. if the RMS error is less than 0.210, the measured surface is classified as a non-defective surface, otherwise, it is classified as a defective surface. As a result, 35 and 1 datasets from the reference surface were classified as non-defective and defective, respectively. On the other hand, 72 and 0 datasets

from the defective surface were classified as defective and non-defective surfaces, respectively. The confusion matrix is shown in table 4. The overall accuracy of the classifier is 99.1%, indicating that the proposed method has good performance for the measured scattering datasets in these experiments. It should be noted that the accuracy is even better than the simulation datasets (89.3%), which may be due to the fact that the actual scattering experiments have a limited number (36) of datasets for each sample compared to those for simulation (5760). Note that the threshold (0.210) was also determined by maximising the accuracy. Compared to the results from simulation (section 3.2), the threshold changed from 0.053 to 0.210, this is due to the fact that the scattering simulation

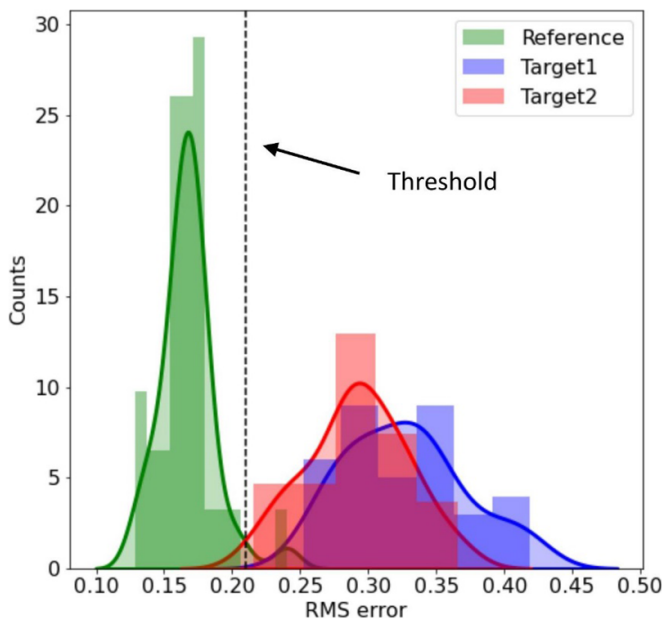


**Figure 15.** Testing results for the AM surfaces using measured scattering data.

**Table 4.** Confusion matrix for the experimental data.

	Predicted:	
	Non-defective	Defective
Actual: Non-defective	35	1
Actual: Defective	0	72

had a limited accuracy which introduced a larger reconstruction error during the encoding-decoding process. Nevertheless, three datasets (one non-defective and two defective) in the experiments can still be discriminated with high accuracy.

The proposed method is based on light scattering and a core algorithm of a convolutional autoencoder, which has the combined advantages of long working distance, and is fast and accurate compared to traditional surface measurement methods such as fringe projection and scanning-based methods (e.g. CSI and focus variation). Most commercial surface measurement systems based on scanning-based methods and fringe projection systems have the processing time in seconds. Some methods can be faster with specific algorithms designed to improve the speed [37]. The processing time of the proposed method is about 60 ms (excluding the image acquisition time), running on a PC with an Intel Xeon CPU (2.20 GHz), using Python as the programming language. Whilst the speed can be further improved by optimising the algorithm and using a faster programming language and binary executable files, it is still relatively fast. It is also faster than the perceptron-like fully connected artificial neural networks developed in our previous work [38], which had processing times of about 100 ms. The proposed method shows accuracies of 89.3% and 99.1% for simulation data and real measurement data, which is promising as it is higher than most methods reported in [39]. The light scattering method also has a working distance. Whilst

the experimental setup had a working distance of 150 mm, it can be easily extended to any practical distance according to the application. This is not the case with scanning-based methods.

#### 4. Conclusions

This paper presents a novel method for quality monitoring of L-PBF process layer surfaces based on using light scattering and unsupervised machine learning. The method has the advantages of being fast, non-contact, operating with a long working distance and without the need for prior knowledge of topography defects. Both simulation and real scattering experiments indicated that the method has high classification accuracy (89.3% and 99.1% accuracies in the confusion matrices, respectively). The testing results obtained in the post-process setup demonstrate the potential of the proposed method and provide an initial promise for future successful implementations in-process and on-machine. Implementation within a commercial L-PBF machine is currently in progress.

#### Data availability statement

The data that support the findings of this study are available upon reasonable request from the authors.

#### Acknowledgments


We acknowledge the support from the Engineering and Physical Sciences Research Council [SPARKLE, EP/R028826/1], European Commission's Horizon 2020 Research and Innovation Staff Exchange Programme [MNR4SCell, 734174], and the University of Nottingham for granting access to the Augusta HPC service.

#### Conflict of interest

The authors declare that they have no known competing financial interests or personal relationships that could have appeared to influence the work reported in this paper.

#### ORCID iDs

Mingyu Liu  <https://orcid.org/0000-0001-8188-9953>

Nicola Senin  <https://orcid.org/0000-0002-9556-0363>

#### References

- [1] Leach R K and Carmignato S 2020 *Precision Metal Additive Manufacturing* (Boca Raton, FL: CRC Press)
- [2] Grasso M L G, Remani A, Dickins A, Colosimo B M and Leach R K 2021 *In-situ* measurement and monitoring methods for metal powder bed fusion—an updated review *Meas. Sci. Technol.* **32** 112001
- [3] Everton S K, Hirsch M, Stravroulakis P, Leach R K and Clare A T 2016 Review of *in-situ* process monitoring and

- in-situ* metrology for metal additive manufacturing *Mater. Des.* **95** 431–45
- [4] Tapia G and Elwany A 2014 A review on process monitoring and control in metal-based additive manufacturing *J. Manuf. Sci. Eng.* **136** 060801
- [5] McCann R et al 2021 *In-situ* sensing, process monitoring and machine control in laser powder bed fusion: a review *Addit. Manuf.* **45** 102058
- [6] Imani F, Gaikwad A, Montazeri M, Rao P, Yang H and Reutzel E 2018 Layerwise in-process quality monitoring in laser powder bed fusion *Proc. ASME 13th Int. Manuf. Sci. Eng. Conf.* p V001T01A38
- [7] Repossini G, Laguzza V, Grasso M and Colosimo B M 2017 On the use of spatter signature for *in-situ* monitoring of laser powder bed fusion *Addit. Manuf.* **16** 35–48
- [8] Caltanissetta F, Grasso M, Petro S and Colosimo B M 2018 Characterization of *in-situ* measurements based on layerwise imaging in laser powder bed fusion *Addit. Manuf.* **24** 183–99
- [9] Clijsters S, Craeghs T, Buls S, Kempen K and Kruth J-P 2014 *In situ* quality control of the selective laser melting process using a high-speed, real-time melt pool monitoring system *Int. J. Adv. Manuf. Technol.* **75** 1089–101
- [10] Furumoto T, Ueda T, Alkahari M R and Hosokawa A 2013 Investigation of laser consolidation process for metal powder by two-color pyrometer and high-speed video camera *CIRP Ann.* **62** 223–6
- [11] Schwerdtfeger J, Singer R F and Körner C 2012 *In situ* flaw detection by IR-imaging during electron beam melting *Rapid Prototyp. J.* **18** 259–63
- [12] Khanzadeh M, Tian W, Yadollahi A, Doude H R, Tschopp M A and Bian L 2018 Dual process monitoring of metal-based additive manufacturing using tensor decomposition of thermal image streams *Addit. Manuf.* **23** 443–56
- [13] Syam W P 2020 In-process surface topography measurements *Advances in Optical Surface Texture Metrology* ed R K Leach (Bristol: IOP Publishing) pp 7-1–7-28
- [14] Leach R K 2011 *Optical Measurement of Surface Topography* (Berlin: Springer)
- [15] Zhang B, Ziegert J, Farahi F and Davies A 2016 *In situ* surface topography of laser powder bed fusion using fringe projection *Addit. Manuf.* **12** 100–7
- [16] Dickins A, Widjanarko T, Sims-Waterhouse D, Thompson A, Lawes S, Senin N and Leach R K 2020 Multi-view fringe projection system for surface topography measurement during metal powder bed fusion *J. Opt. Soc. Am. A* **37** B93–B105
- [17] Afazov S, Okioga A, Holloway A, Denmark W, Triantaphyllou A, Smith S-A and Bradley-Smith L 2017 A methodology for precision additive manufacturing through compensation *Precis. Eng.* **50** 269–74
- [18] Kalms M, Narita R, Thomy C, Vollertsen F and Bergmann R B 2019 New approach to evaluate 3D laser printed parts in powder bed fusion-based additive manufacturing in-line within closed space *Addit. Manuf.* **26** 161–5
- [19] Jayasinghe S, Paoletti P, Sutcliffe C, Dardis J, Jones N and Green P L 2022 Automatic quality assessments of laser powder bed fusion builds from photodiode sensor measurements *Prog. Addit. Manuf.* **7** 143–60
- [20] Okaro I A, Jayasinghe S, Sutcliffe C, Black K, Paoletti P and Green P L 2019 Automatic fault detection for laser powder-bed fusion using semi-supervised machine learning *Addit. Manuf.* **27** 42–53
- [21] Coeck S, Bisht M, Plas J and Verbist F 2019 Prediction of lack of fusion porosity in selective laser melting based on melt pool monitoring data *Addit. Manuf.* **25** 347–56
- [22] Remani A, Williams R, Thompson A, Dardis J, Jones N, Hooper P and Leach R K 2021 Design of a multi-sensor measurement system for *in-situ* defect identification in metal additive manufacturing *Proc. Euspen Advancing Precision in Additive Manufacturing*
- [23] Liu M, Fai Cheung C, Senin N, Wang S, Su R and Leach R K 2020 On-machine surface defect detection using light scattering and deep learning *J. Opt. Soc. Am. A* **37** B53–B9
- [24] Liu M, Senin N and Leach R K 2019 Defect detection for structured surfaces via light scattering and machine learning *Proc. 14th Int. Symp. On Measurement Technology and Intelligent Instruments (ISMTI2019)*
- [25] Liu M, Senin N, Su R and Leach R K 2020 Cascaded machine learning model for reconstruction of surface topography from light scattering *Proc. SPIE* **11352** 113520Q
- [26] Paz V F, Peterhänsel S, Frenner K and Osten W 2012 Solving the inverse grating problem by white light interference Fourier scatterometry *Light Sci. Appl.* **1** e36–e
- [27] Liu M, Senin N and Leach R K 2021 Intelligent quality monitoring for additive manufactured surfaces by machine learning and light scattering *Proc. SPIE* **11782** 1178206
- [28] Liu M, Senin N and Leach R K 2021 Fast measurement of metal laser powder bed fusion layer surfaces using light scattering and principal component analysis euspen SIG
- [29] Coupland J M and Nikolaev N I 2019 A new approach to vector scattering: the 3s boundary source method *Opt. Express* **27** 30380–95
- [30] de Groot P 2011 Coherence scanning interferometry *Optical Measurement of Surface Topography* ed R K Leach (Berlin: Springer) pp 187–208
- [31] Su R, Coupland J, Sheppard C and Leach R K 2021 Scattering and three-dimensional imaging in surface topography measuring interference microscopy *J. Opt. Soc. Am. A* **38** A27–A42
- [32] Su R and Leach R K 2021 Physics-based virtual coherence scanning interferometer for surface measurement *Light Adv. Manuf.* **2** 120-135
- [33] Beckmann P and Spizzichino A 1987 *The Scattering of Electromagnetic Waves from Rough Surfaces* (Norwood, MA: Artech House)
- [34] Simonsen I 2010 Optics of surface disordered systems *Eur. Phys. J. Spec. Top.* **181** 1–103
- [35] Thomas M, Su R, Nikolaev N, Coupland J and Leach R K 2020 Modeling of interference microscopy beyond the linear regime *Opt. Eng.* **59** 034110
- [36] Rudemo M 1982 Empirical choice of histograms and kernel density estimators *Scan. J. Stat.* **9** 65–78
- [37] Zhang S 2010 Recent progresses on real-time 3D shape measurement using digital fringe projection techniques *Opt. Lasers Eng.* **48** 149–58
- [38] Liu M, Senin N and Leach R K 2022 Measurement of laser-based powder bed fusion surfaces using light scattering and one-class support vector machines *Proc. SPIE* **12137** 12137–7
- [39] Fu Y, Downey A R, Yuan L, Zhang T, Pratt A and Balogun Y 2022 Machine learning algorithms for defect detection in metal laser-based additive manufacturing: a review *J. Manuf. Process.* **75** 693–710